energies

MDPI

Article

Medium-Frequency Oscillation in Voltage-Controlled Full-Bridge Inverter with a Nonlinear Inductor

Faqiang Wang [1,*], Hongwei Zhou [1,2], Jiansong Zhang [1,2] and Hongbo Cao [1]

[1] State Key Laboratory of Electrical Insulation and Power Equipment, School of Electrical Engineering, Xi'an Jiaotong University, Xi'an 710049, China; zhouhongwei@stu.xjtu.edu.cn (H.Z.); zjs2013@stu.xjtu.edu.cn (J.Z.); caohongbo@stu.xjtu.edu.cn (H.C.)
[2] TBEA Xi'an Electric Technology Co., Ltd., Xi'an 710119, China
* Correspondence: faqwang@mail.xjtu.edu.cn; Tel.: +29-82668630-218

Abstract: An inverter, whose inductor current is periodic, is the key equipment for photovoltaic power generation, fuel cell power generation, etc. A nonlinear inductor, whose inductance will be changed by its current, can be used to improve the grid current quality of the inverter, although making the mathematical model of the inverter system more complex. In this paper, the voltage-controlled full-bridge inverter with a nonlinear inductor is investigated and its mathematical model is established. The influence of parameters on the dynamical behaviors of this system is analyzed by using the harmonic balance method and the Floquet theory. Consequently, the mechanism for the occurrence of medium-frequency oscillation is revealed. The hardware circuit for the voltage-controlled full-bridge inverter with a nonlinear inductor is designed and some experimental results are presented for confirmation. The research results show that the mechanism for the occurrence of medium-frequency oscillation is Hopf bifurcation and its oscillation frequency is between the line frequency and the switching frequency.

Keywords: full-bridge inverter; mathematical model; medium-frequency oscillation; Hopf bifurcation

Citation: Wang, F.; Zhou, H.; Zhang, J.; Cao, H. Medium-Frequency Oscillation in Voltage-Controlled Full-Bridge Inverter with a Nonlinear Inductor. *Energies* **2021**, *14*, 3848. https://doi.org/10.3390/en14133848

Academic Editor: Alon Kuperman

Received: 26 April 2021
Accepted: 18 June 2021
Published: 25 June 2021

1. Introduction

Switching power converters, which include DC–DC converters, power factor correction (PFC) converters, DC–AC inverters, etc., mainly consist of semiconductors, inductors, capacitors, and loads, and have been widely employed in practical engineering systems such as photovoltaic (PV) power generation, fuel cell power generation, etc. [1]. For inductors in the switching power converters, as indicated in [2,3], two aspects need to be considered. (1) In order to reduce the THD of the system's current and improve the whole system's efficiency, the inductor needs to have a sufficiently high inductance under light-load current. (2) Under heavy-load current, it is hoped that the designed inductor would have low inductance to ensure that the inductor is in an unsaturated state. Obviously, it will be difficult for linear inductors to satisfy both these requirements simultaneously. In order to solve this problem, the nonlinear inductor has been proposed and designed [3–8]. For example, a ladder-gap nonlinear inductor whose inductance can be varied with the specified load was designed in [3]. Based on low-temperature co-fired ceramic (LTCC) technology, the multiwindow multipermeability nonlinear LTCC inductor was fabricated and applied to a DC–DC buck converter in [4]. In [5], the nonlinear inductor was employed in the interleaved power factor correction (PFC) converter, its Jiles–Atherton model was established, and the dynamic behaviors of the system were investigated. In [6], efficient nonlinear inductors were adopted in PV inverters and active PFC converters; the corresponding design method for nonlinear inductors was presented, where the research results showed its ability to perform at a size 32% smaller than linear inductors, with 20% less copper, and a total power loss that is 10% lower by using nonlinear inductors instead of linear inductors in a practical PV inverter. Furthermore, some researchers have applied

nonlinear inductors to the three-phase grid-connected inverter [7], single-phase PV grid converters [8], DC–DC boost converters [9], and so on. Certainly, the research results above have greatly promoted the design of nonlinear inductors and their applications in switching power converters.

In addition, the extant research results in [10–18] show that the inverter is a type of strongly nonlinear system so that there are rich and complex nonlinear phenomena which will inevitably have an important influence on the performance of the inverter. For instance, in [10], bifurcation and chaos in the single-phase sinusoidal pulse width modulation (SPWM) full-bridge inverter with a linear inductor were analyzed by using the discrete model, and an adaptive carrier amplitude modulation control method was presented to control these discovered instabilities in order to ensure its stable operation. In [11], the exponential delay feedback control method used for controlling the chaotic phenomenon in the single-phase H-bridge photovoltaic inverter with a linear inductor was reported. In [12], the fast-scale instability and slow-scale instability in a single-phase parallel full-bridge inverter with a linear inductor was analyzed. Likewise, the complex nonlinear phenomena of the dual buck full-bridge inverter with a linear inductor were studied in [13]. The bifurcation phenomenon in parallel-connected voltage-source inverters with a linear inductor was analyzed by using the delay-feedback control method in [15]. The above research results provide good guidance for the parameter design of the inverter system in practical engineering to ensure its stable operation.

These achievements were all carried out on inverters with linear inductors; that is, the mathematical model of the inverter systems are piecewise linear models so that the analytical solution in each segment could be obtained, and the discrete model could be used to analyze such systems. However, with the introduction of the nonlinear inductor whose characteristics will make the dynamic behaviors of the inverter system more complicated, analyzing its strongly nonlinear system with the use of the discrete model will certainly prove to be even more difficult. Therefore, it is necessary to study the inverter with a nonlinear inductor that aims to provide a theoretical basis and design guidance for its engineering applications.

In this paper, the mathematical model of the voltage-controlled full-bridge inverter with a nonlinear inductor is established, the influence of system's parameters on its dynamic behaviors is analyzed, and the mechanism of medium frequency oscillation in the system is revealed. Additionally, a hardware circuit for the system is designed, and some experimental results used to verify the correctness of the theoretical analyses and the existence of the medium-frequency oscillation phenomenon are presented.

2. Nonlinear Inductor's Model and Its Experimental Verification

For the nonlinear inductor, its inductance can be described by its static inductance and dynamic inductance [3]. The mathematical model for the nonlinear inductor's static inductance, provided in the system-level power electronics simulation software and named Piecewise Linear Electrical Circuit Simulation (PLECS) developed by the Swiss company Plexim GmbH, is given as [19]:

$$L_E = \mathrm{A}_1 + \mathrm{A}_2 \frac{\arctan(\mathrm{A}_3 i_N)}{i_N} \tag{1}$$

where A_1, A_2, and A_3 are the parameters of the nonlinear inductor, arctan is the arctangent function, i_N is the current through the nonlinear inductor, and L_E is the static inductance of the nonlinear inductor.

Note that the expression for the magnetic flux linkage of the nonlinear inductor is φ; $= L_E i_N$, i.e., $\varphi = \mathrm{A}_1 i_N + \mathrm{A}_2 \arctan(\mathrm{A}_3 i_N)$. Subsequently, the voltage across this nonlinear

inductor is $v_{LN} = d\varphi/dt$, that is, the relationship between the current i_N through this nonlinear inductor and its voltage v_{LN} satisfies the following formula:

$$v_{LN} = \frac{A_1+A_2A_3+A_1A_3{}^2i_N{}^2}{1+A_3{}^2i_N{}^2}\frac{di_N}{dt} \tag{2}$$

Additionally, based on the definition of dynamic inductance L_N, its expression is the following:

$$L_N = \frac{d\varphi}{di_N} = \frac{A_1+A_2A_3+A_1A_3{}^2i_N{}^2}{1+A_3{}^2i_N{}^2} \tag{3}$$

The test circuit consisting of an AC voltage source $v_S(t)$, linear resistor R, nonlinear inductor L_N, and linear inductor L is shown in Figure 1a, where $R = 1\ \Omega$, $L = 110\ \mu$H, and $v_S(t) = 18\sin(2000\pi t)$V. Notably, L_N is the dynamic inductance of the nonlinear inductor. According to Figure 1a, the experimental test data including the voltage across the linear inductor v_L, the voltage across the nonlinear inductor v_{LN}, and the voltage across the linear resistor v_R can be obtained. Additionally, since the linear resistor is $R = 1\ \Omega$, the current i_N through the nonlinear inductor can be represented by the voltage v_R. Thus, the dynamic inductance of the nonlinear inductor can be calculated as follows:

$$L_N = L\frac{v_{LN}}{v_L} \tag{4}$$

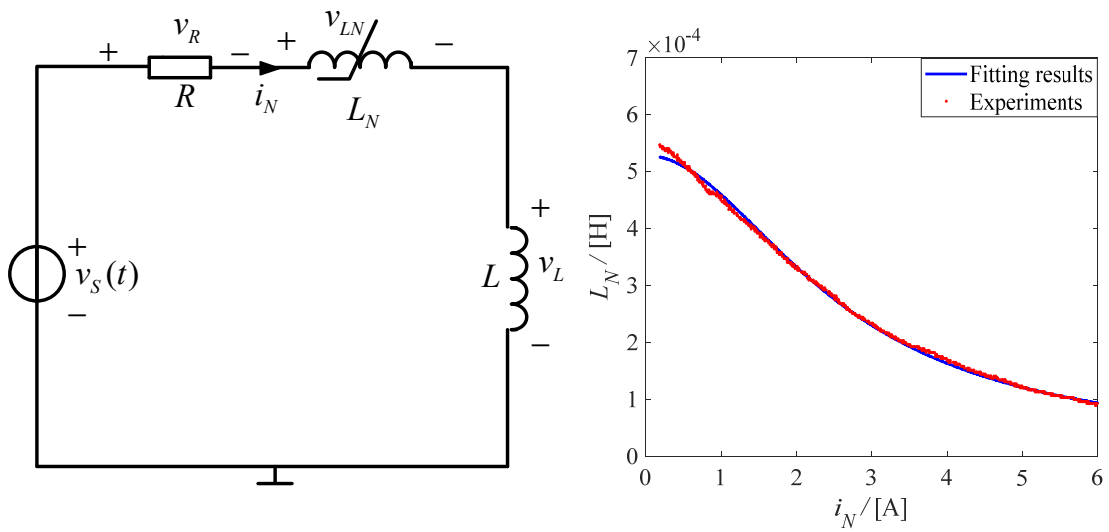

(**a**) (**b**)

Figure 1. Test circuit of nonlinear inductor. (**a**) Circuit diagram, (**b**) Comparisons of nonlinear inductor fitting results and experiments.

By making the dynamic inductance L_N described in (3) as the goal of the fitting function and substituting the test data obtained from the experiments in (3), A_1, A_2, and A_3 shown in (3) could be obtained by using the nlinfit function in the Matlab software; the fitting results are $A_1 = 1.5845 \times 10^{-5}$, $A_2 = 0.0013$, and $A_3 = 0.3932$. Figure 1b shows the comparisons between the fitted nonlinear inductance L_N with the current i_N and the corresponding experimental test results. One can see that the results from these two sides are basically consistent with each other, indicating the effectiveness of the nonlinear inductor model and the correctness of the fitting technique.

3. Mathematical Model and Approximate Calculation

By replacing the linear inductor in the full-bridge inverter with the above-mentioned nonlinear inductor L_N, the circuit schematic diagram of the voltage-controlled full-bridge

inverter with nonlinear inductor L_N could be obtained and is shown in Figure 2. The power circuit of this system consists of an input DC voltage v_{in}, four power switches (Q_1, Q_2, Q_3, and Q_4), a nonlinear inductor L_N (whose inductor current is i_N), a linear capacitor C (whose voltage is v_0), and a load resistor R_L. Note that four power switches (Q_1, Q_2, Q_3, and Q_4) form the inverter bridge, and they are turned on or off by their drive signals. Specifically, when the drive signal is at a high level, the corresponding power switches are turned on, otherwise they are turned off. Moreover, the driving signals of Q_1 and Q_4 are the same, the driving signals of Q_2 and Q_3 are the same, and Q_1 and Q_2 are turned on complementarily.

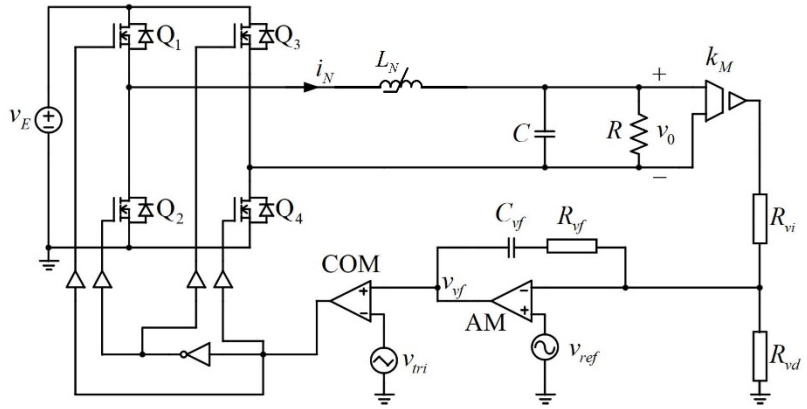

Figure 2. Schematic diagram of the voltage-controlled full-bridge inverter with nonlinear inductor.

The control circuit of this system is composed of the measurement circuit for the output floating voltage v_0, the bleeder circuit consisting of R_{vi} and R_{vd}, the PI compensator, the SPWM generator, and the driving circuit. The output voltage of the PI compensator is v_{vf} and $v_{ref} = V_{ref}\sin(\omega_0 t)$. Assuming that all components are ideal, i.e., their parasitic parameters are not considered since their values are very small, taking the voltage v_0, the current i_N, and the voltage v_{vf} as the circuit variables, and based on the KCL and KVL law, the mathematical model of the system described by differential equations can be obtained as follows:

$$\begin{cases} \frac{di_N}{dt} = \frac{1+A_3{}^2 i_N{}^2}{A_1+A_2A_3+A_1A_3{}^2 i_N{}^2}((2S-1)v_E - v_0) \\ \frac{dv_0}{dt} = \frac{i_N}{C} - \frac{v_0}{R_L C} \\ \frac{dv_{vf}}{dt} = \frac{k_M R_{vf} v_0}{R_{vi} C R_L} - \frac{k_M v_0}{R_{vi} C_{vf}} - \frac{k_M R_{vf} i_N}{R_{vi} C} + k_1 \sin(\omega_0 t) + k_2 \cos(\omega_0 t) \end{cases} \tag{5}$$

where

$$\begin{cases} k_1 = (\frac{1}{R_{vi}} + \frac{1}{R_{vd}})\frac{V_{ref}}{C_{vf}} \\ k_2 = (\frac{R_{vf}}{R_{vi}} + \frac{R_{vf}}{R_{vd}} + 1)V_{ref}\omega_0 \end{cases} \tag{6}$$

Notably, $S = 1$ means that Q_1 and Q_4 are turned on, while Q_2 and Q_3 are turned off. $S = 0$ means that Q_2 and Q_3 are turned on, while Q_1 and Q_4 are turned off. Clearly different from the full-bridge inverter with a linear inductor, Equation (5) is always nonlinear for both $S = 1$ and $S = 0$ so that it will be difficult to obtain its analytical solution, and the discrete model cannot be adopted to analyze the stability of the voltage-controlled full-bridge inverter with a nonlinear inductor.

As for the bipolar SPWM generator, it consists of a comparator COM, a triangular carrier v_{tri}, and a power switch driver. Note that the triangle carrier v_{tri} is expressed as follows:

$$v_{tri} = \begin{cases} -(\omega_{sw}t - 2\pi k - 2\pi)\frac{2V_{tri}}{\pi} - V_{tri}, \ 2\pi k + \pi \le \omega_{sw}t \le 2\pi k + 2\pi \\ (\omega_{sw}t - 2\pi k)\frac{2V_{tri}}{\pi} - V_{tri}, \ 2\pi k \le \omega_{sw}t \le 2\pi k + \pi \end{cases} \tag{7}$$

where ω_{sw} and V_{tri} are the angular frequency and the amplitude of the triangular carrier, respectively. The triangle carrier v_{tri} is compared with the voltage v_{vf} to generate the SPWM signal. If $v_{tri} < v_{vf}$, the comparator COM output is at a high level, while if $v_{tri} > v_{vf}$, the comparator COM outputs a low level.

For the full-bridge inverter with a nonlinear inductor, the angular frequency ω_{sw} of the triangular carrier v_{tri} is much larger than the angular frequency ω_0 of the modulating wave v_{ref}; that is, the switching frequency f_{sw}($f_{sw} = \omega_{sw}/2\pi$) is much larger than the power frequency f_0($f_0 = \omega_0/2\pi$). Therefore, the average modeling method proposed in [20] can be used to establish the average model of the system, and the duty ratio $\langle d \rangle$ can be computed as follows:

$$d = \frac{1}{2}\left(1 + \frac{\left\langle v_{vf} \right\rangle}{V_{tri}}\right) \tag{8}$$

Therefore, the average model of the voltage-controlled full-bridge inverter with a nonlinear inductor can be given as:

$$\begin{cases} \frac{d\langle i_N \rangle}{dt} = \frac{1+A_3{}^2\langle i_N \rangle^2}{A_1+A_2A_3+A_1A_3{}^2\langle i_N \rangle^2}\left(\frac{v_E}{V_{tri}}\langle v_{vf} \rangle - \langle v_0 \rangle\right) \\ \frac{d\langle v_0 \rangle}{dt} = \frac{\langle i_N \rangle}{C} - \frac{\langle v_0 \rangle}{R_L C} \\ \frac{d\left\langle v_{vf} \right\rangle}{dt} = \frac{k_M R_{vf}\langle v_0 \rangle}{R_{vi} C R_L} - \frac{k_M \langle v_0 \rangle}{R_{vi} C_{vf}} - \frac{k_M R_{vf}\langle i_N \rangle}{R_{vi} C} + k_1 \sin(\omega_0 t) + k_2 \cos(\omega_0 t) \end{cases} \tag{9}$$

where $\langle d \rangle$, $\langle i_N \rangle$, $\langle v_0 \rangle$, and $\langle v_{vf} \rangle$ are the average values of d, i_N, v_0, and v_{vf} in one switching period, respectively.

One can see that the voltage-controlled full-bridge inverter with a nonlinear inductor described by (9) is a complex nonlinear and non-autonomous circuit system. Generally speaking, for this inverter system, it is expected that the average value of its output voltage v_0 should be approximately a sine wave, and the harmonic is expected to be as low as possible; therefore, it can be assumed as:

$$\langle v_0 \rangle = a_0 + \sum_{n=1}^{N} [a_n \cos(n\tau) + b_n \sin(n\tau)] \tag{10}$$

where $\tau = \omega_0 t$ and

$$\begin{cases} \langle v'_0 \rangle = \frac{d\langle v_0 \rangle}{dt} \\ \langle v''_0 \rangle = \frac{d^2\langle v_0 \rangle}{dt^2} \\ \langle v_0 \rangle^{(-1)} = \int \langle v_0 \rangle dt \end{cases} \tag{11}$$

hence,

$$\begin{cases} \langle i_N \rangle = C\langle v\prime_0 \rangle + \langle v_0 \rangle / R_L \\ \langle v_{vf} \rangle = \frac{V_{tri}}{v_E}\left(\langle i\prime_N \rangle \frac{(A_1+A_2A_3)+A_1A_3{}^2\langle i_N \rangle^2}{1+A_3{}^2\langle i_N \rangle^2} + \langle v_0 \rangle\right) \\ \langle i\prime_N \rangle = C\langle v\prime\prime_0 \rangle + \langle v\prime_0 \rangle / R_L \end{cases} \tag{12}$$

By substituting the first expression and the third expression of (12) with (9), we can get the following:

$$\begin{aligned} &f(a_0, a_1, \ldots, a_N, b_1, \ldots, b_N) = (A_1+A_2A_3+A_1A_3{}^2(C\langle v'_0 \rangle + \tfrac{\langle v_0 \rangle}{R_L})^2) \\ &(C\langle v''_0 \rangle + \tfrac{\langle v'_0 \rangle}{R_L}) - (1 + A_3{}^2(C\langle v'_0 \rangle + \tfrac{\langle v_0 \rangle}{R_L})^2)(\tfrac{v_E}{V_{tri}}(\tfrac{k_M R_{vf}\langle v_0 \rangle^{(-1)}}{R_{vi} C R_L} \\ &- \tfrac{k_M \langle v_0 \rangle^{(-1)}}{R_{vi} C_{vf}} - \tfrac{k_M R_{vf}(C\langle v_0 \rangle + \langle v_0 \rangle^{(-1)}/R_L)}{R_{vi} C} - \tfrac{k_1}{\omega_0}\cos(\tau) + \tfrac{k_2}{\omega_0}\sin(\tau)) - \langle v_0 \rangle) \end{aligned} \tag{13}$$

Notably, if the bigger number N is selected, more accurate results can be obtained. However, by considering that the amplitudes of high order harmonics are very small when compared to that of the fundamental, choosing a small value for N is enough. Then,

substituting (10) and (11) with (13) and taking $N = 4$, and based on the principle of harmonic balance, we can get the following:

$$\begin{cases} \int_0^{2\pi} f(a_0,a_1,a_2,a_3,a_4,b_1,b_2,b_3,b_4)d\tau = 0 \\ \int_0^{2\pi} f(a_0,a_1,a_2,a_3,a_4,b_1,b_2,b_3,b_4)\cos(\tau)d\tau = 0, \int_0^{2\pi} f(a_0,a_1,a_2,a_3,a_4,b_1,b_2,b_3,b_4)\cos(2\tau)d\tau = 0 \\ \int_0^{2\pi} f(a_0,a_1,a_2,a_3,a_4,b_1,b_2,b_3,b_4)\cos(3\tau)d\tau = 0, \int_0^{2\pi} f(a_0,a_1,a_2,a_3,a_4,b_1,b_2,b_3,b_4)\cos(4\tau)d\tau = 0 \\ \int_0^{2\pi} f(a_0,a_1,a_2,a_3,a_4,b_1,b_2,b_3,b_4)\sin(\tau)d\tau = 0, \int_0^{2\pi} f(a_0,a_1,a_2,a_3,a_4,b_1,b_2,b_3,b_4)\sin(2\tau)d\tau = 0 \\ \int_0^{2\pi} f(a_0,a_1,a_2,a_3,a_4,b_1,b_2,b_3,b_4)\sin(3\tau)d\tau = 0, \int_0^{2\pi} f(a_0,a_1,a_2,a_3,a_4,b_1,b_2,b_3,b_4)\sin(4\tau)d\tau = 0 \end{cases} \quad (14)$$

By solving (14), the coefficients a_0, a_1, a_2, a_3, a_4, b_1, b_2, b_3, and b_4 can be calculated by using the improved differential evolution method, and the expression for the average output voltage $\langle v_0 \rangle$ of the voltage-controlled full-bridge inverter with a nonlinear inductor can be obtained.

The circuit parameters of the voltage-controlled full-bridge inverter with a nonlinear inductor are chosen as v_E = 12 V, C = 20 µF, R_L = 5 Ω, V_{tri} = 2 V, V_{ref} = 1 V, f_{sw} = 25 kHz, f_0 = 50 Hz, C_{vf} = 102 nF, R_{vf} = 1 kΩ, R_{vi} = 36 kΩ, R_{vd} = 36 kΩ, and k_M = 0.25. The approximate solution of the voltage $\langle v_0 \rangle$ is calculated as:

$$\begin{aligned} \langle v_0 \rangle = \quad & -0.187207 - 1.263136\cos(\tau) + 7.158382\sin(\tau) \\ & -0.100880\cos(2\tau) - 0.178769\sin(2\tau) - 0.057748\cos(3\tau) \\ & -0.137595\sin(3\tau) - 0.018889\cos(4\tau) - 0.109892\sin(4\tau) \end{aligned} \quad (15)$$

Likewise, the current $\langle i_N \rangle$ and the voltage $\langle v_{vf} \rangle$ from (12) can be obtained.

Figure 3 shows the comparisons between the numerical simulations obtained from (9) and the approximate calculation results obtained from the harmonic balance (HB) method. It can be seen that the results from these two sides are consistent with each other, which indicates that the harmonic balance method is effective for calculating the approximate solution of the voltage-controlled full-bridge inverter with a nonlinear inductor.

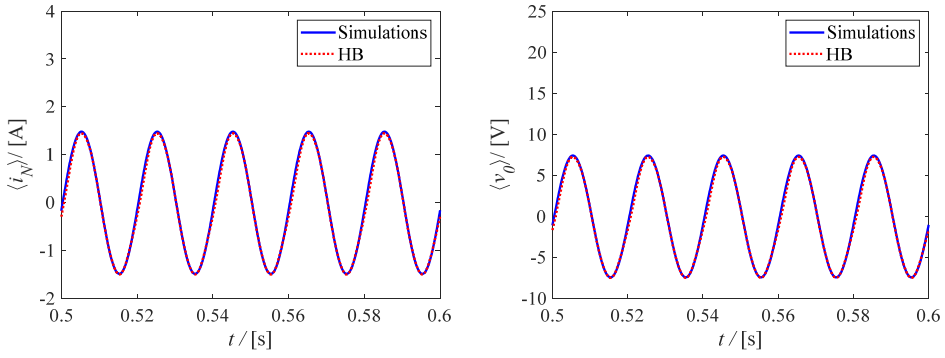

(**a**) (**b**)

Figure 3. Comparison of numerical simulations and the results from HB. (**a**) $\langle i_N \rangle$; (**b**) $\langle v_0 \rangle$.

4. Theoretical Analysis on Oscillation Phenomena

From (9), it can be seen that the voltage-controlled full-bridge inverter with a nonlinear inductor is a type of periodic time-varying nonlinear non-autonomous system, and its solution is the periodic solution as shown in (15). Therefore, the Floquet theory can be used

to judge the stability of the periodic solution descried in (15). Supposing that this system has a small perturbation near its periodic solution, the following equation can be used:

$$\begin{cases} i_N = \langle i_N \rangle + \Delta i_N \\ v_0 = \langle v_0 \rangle + \Delta v_0 \\ v_{vf} = \left\langle v_{vf} \right\rangle + \Delta v_{vf} \end{cases} \tag{16}$$

where

$$\begin{cases} \langle i_N \rangle \gg \Delta i_N \\ \langle v_0 \rangle \gg \Delta v_0 \\ \left\langle v_{vf} \right\rangle \gg \Delta v_{vf} \end{cases}$$

Then, linearize (9) at its periodic solution ($\langle i_N \rangle$, $\langle v_0 \rangle$, $\langle v_{vf} \rangle$), the linearization matrix $\mathbf{Y}(\tau)$ can be obtained as follows:

$$\mathbf{Y}(\tau) = \begin{bmatrix} \frac{a_{11}}{\omega_0} & \frac{a_{12}}{\omega_0} & \frac{a_{13}}{\omega_0} \\ \frac{1}{\omega_0 C} & -\frac{1}{\omega_0 R_L C} & 0 \\ -\frac{k_M R_{vf}}{\omega_0 R_{vi} C} & \frac{k_M R_{vf}}{\omega_0 R_{vi} C R_L} - \frac{k_M}{\omega_0 R_{vi} C_{vf}} & 0 \end{bmatrix} \tag{17}$$

where

$$\begin{cases} a_{11} = (\frac{v_E}{V_{tri}} \langle v_{vf} \rangle - \langle v_0 \rangle)(\frac{2A_3{}^2 \langle i_N \rangle}{A_1 + A_2 A_3 + A_1 A_3{}^2 \langle i_N \rangle^2} - \frac{2A_1 A_3{}^2 \langle i_N \rangle (1 + A_3{}^2 \langle i_N \rangle^2)}{(A_1 + A_2 A_3 + A_1 A_3{}^2 \langle i_N \rangle^2)^2}) \\ a_{12} = -\frac{1 + A_3{}^2 \langle i_N \rangle^2}{A_1 + A_2 A_3 + A_1 A_3{}^2 \langle i_N \rangle^2} \\ a_{13} = \frac{1 + A_3{}^2 \langle i_N \rangle^2}{A_1 + A_2 A_3 + A_1 A_3{}^2 \langle i_N \rangle^2} \frac{v_E}{V_{tri}} \end{cases} \tag{18}$$

The period of the linearization matrix $\mathbf{Y}(\tau)$ is consistent with the period of $\langle v_0 \rangle$. Therefore, the linearized system can be expressed as follows:

$$\dot{\mathbf{x}} = \mathbf{Y}(\tau) x, \quad \mathbf{x} = (\Delta i_N; \Delta v_0; \Delta v_{vf}) \in R^3 \tag{19}$$

If $\Phi(\tau)$ is the periodic solution of (19), then $\Phi(\tau + T)$ is also the periodic solution of (19), and there is the following:

$$\Phi(\tau + T) = \mathbf{M}\Phi(\tau) \tag{20}$$

where $\mathbf{M}$ is the transition matrix. Let $\tau = 0$ and $\Phi(0) = I$, and there is the following:

$$\mathbf{M} = \Phi(T) \tag{21}$$

According to the Floquet theory, if the Floquet multipliers of the transition matrix $\mathbf{M}$ are all located in the unit circle, the periodic time-varying system is stable [21]. Otherwise,

- If one of the Floquet multipliers of the transition matrix $\mathbf{M}$ passes through the unit circle from the negative real axis and the rest remains in the unit circle, the period-doubling bifurcation occurs in the periodic time-varying system;
- If one of the Floquet multipliers of the transition matrix $\mathbf{M}$ passes through the unit circle from the positive real axis and the rest remains in the unit circle, the pitch-fork bifurcation occurs in the periodic time-varying system;
- If a pair of conjugate Floquet multipliers of the transition matrix $\mathbf{M}$ goes out of the unit circle and the rest remains in the unit circle, then Hopf bifurcation occurs in the periodic time-varying system.

Since the period of τ is 2π, that is $T = 2\pi$. Divide T into equal subparts N_k, then $t_k = T_k/N_k$. This is defined as follows:

$$\mathbf{Y}_k = \frac{1}{\Delta k}\int_{t_{k-1}}^{t_k} \mathbf{Y}(\tau)d\tau \tag{22}$$

Hence, the transition matrix $\mathbf{M}$ can be given as follows:

$$\begin{aligned}\mathbf{M} &= \prod_{i=N_k}^{1}[\exp(\mathbf{Y}_i\Delta_i)] \\ &= \exp(\mathbf{Y}_{N_k}\Delta_{N_k})\exp(\mathbf{Y}_{N_k-1}\Delta_{N_k-1})\ldots\exp(\mathbf{Y}_1\Delta_1) \\ &= \prod_{i=N_k}^{1}\left[\mathbf{I} + \sum_{j=1}^{N_j}\frac{(\mathbf{Y}_i\Delta_i)^j}{j!}\right]\end{aligned} \tag{23}$$

where

$$\mathbf{Y}_k = \begin{bmatrix} \frac{1}{\omega_0}\frac{1}{\Delta k}\int_{t_{k-1}}^{t_k} a_{11}d\tau & \frac{1}{\omega_0}\frac{1}{\Delta k}\int_{t_{k-1}}^{t_k} a_{12}d\tau & \frac{1}{\omega_0}\frac{1}{\Delta k}\int_{t_{k-1}}^{t_k} a_{13}d\tau \\ \frac{1}{\omega_0 C} & -\frac{1}{R_L\omega_0 C} & 0 \\ -\frac{k_M R_{vf}}{\omega_0 R_{vi} C} & \frac{k_M R_{vf}}{\omega_0 R_{vi} C R_L} - \frac{k_M}{\omega_0 R_{vi} C_{vf}} & 0 \end{bmatrix} \tag{24}$$

According to (23), the Floquet multiplier of the transition matrix $\mathbf{M}$ can be calculated and used to determine the stability and bifurcation types of the periodic time-varying system. With the selected parameters in the previous section and the periodic solution obtained in (15), three Floquet multiples of the transition matrix $\mathbf{M}$ are calculated as $\lambda_1 = 2.9667 \times 10^{-4}$, $\lambda_2 = 2.6986 \times 10^{-21}$, and $\lambda_3 = -2.0678 \times 10^{-20}$, respectively. Evidently, these three Floquet multiples remain in the unit circle, indicating that the voltage-controlled full-bridge inverter with a nonlinear inductor is in stable operation.

The variations of three Floquet multipliers of the transition matrix $\mathbf{M}$ with respect to the different capacitor C_{vf} in the PI compensator are shown in Table 1. Additionally, two Floquet multiples (λ_2 andλ_3) with different capacitors C_{vf} are plotted in Figure 4. From Table 1 and Figure 4, when $C_{vf} = 4$ nF, three Floquet multiples (a real number and a pair of complex conjugates) of the transition matrix $\mathbf{M}$ of the voltage-controlled full-bridge inverter with a nonlinear inductor are all located in the unit circle, indicating that this system is stable. However, when $C_{vf} = 3.9$ nF, a pair of conjugate complex Floquet multiples of the transition matrix $\mathbf{M}$ are located outside the unit circle, indicating that the voltage-controlled full-bridge inverter with a nonlinear inductor is in unstable operation. Therefore, when the capacitor C_{vf} gradually decreases from 4 nF to 3.9 nF, there is a pair of complex conjugate Floquet multipliers penetrating from inside the unit circle and moving outwards, that is, Hopf bifurcation is occurring in this system. Therefore, when $C_{vf} \geq 4$ nF, the voltage-controlled full-bridge inverter with a nonlinear inductor is stable, while when C_{vf} is less than or equal to 3.9 nF, the system is unstable.

Table 1. Floquet multipliers of the transition matrix $\mathbf{M}$ with respect to the different values of C_{vf}.

$\mathbf{C_{vf}}$	$\boldsymbol{\lambda_1}$	$\boldsymbol{\lambda_{2,3}}$	$\boldsymbol{\lvert\lambda_{2,3}\rvert}$	**State**
120.0nF	0.0010	-5.7784×10^{-20}, -2.8184×10^{-20}	Less than 0.01	Stable
100.0nF	0.0003	-4.1838×10^{-21}, 7.4738×10^{-21}	Less than 0.01	Stable
80.0nF	2.8828×10^{-5}	$-3.9112 \times 10^{-22} \pm 3.3437 \times 10^{-22}i$	Less than 0.01	Stable
60.0nF	7.2088×10^{-7}	-2.2764×10^{-23}, 3.3481×10^{-23}	Less than 0.01	Stable
40.0nF	3.2698×10^{-10}	$-1.1158 \times 10^{-26} \pm 5.6199 \times 10^{-26}i$	Less than 0.01	Stable
20.0nF	2.5304×10^{-21}	$-1.5602 \times 10^{-35} \pm 7.3916 \times 10^{-34}i$	Less than 0.01	Stable
10.0nF	-1.5264×10^{-37}	$-4.8659 \times 10^{-22} \pm 1.8747 \times 10^{-22}i$	Less than 0.01	Stable
4.0nF	-1.3293×10^{-16}	$-0.9869 \pm 0.1610i$	0.9999	Stable
3.9nF	-4.9487×10^{-16}	$-1.7504 \pm 3.5006i$	3.9139	Unstable

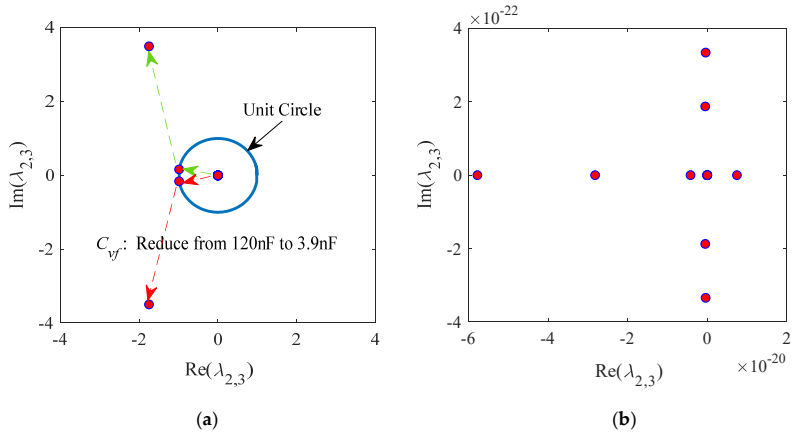

Figure 4. Changing trajectory of the eigenvalues $\lambda_{2,3}$ with respect to different C_{vf} in the complex plane. (**a**) The eigenvalues $\lambda_{2,3}$ corresponding to Table 1 and (**b**) close-up view near the origin.

Therefore, when C_{vf} = 102 nF and its value is greater than 4 nF, the voltage-controlled full-bridge inverter with a nonlinear inductor should be stable and there is no oscillation in the current i_N and the voltage v_0, as shown in Figure 3. However, when C_{vf} = 2 nF and its value is less than 3.9 nF, the voltage-controlled full-bridge inverter with a nonlinear inductor is unstable. The calculated three Floquet multipliers of the corresponding transition matrix **M** under C_{vf} = 2 nF are λ_1 = 1.1686 and $\lambda_{2,3} = 3.2608 \times 10^{16} \pm 7.2821 \times 10^{15} i$, respectively. It can be seen that these three Floquet multipliers are located outside of the unit circle, which further proves that the voltage-controlled full-bridge inverter with a nonlinear inductor under C_{vf} = 2 nF is indeed unstable.

Figure 5 shows the stability boundaries in the parameter space of the capacitor C_{vf} and the capacitor C. One can see that with the decrease of capacitance C_{vf} or the increase of capacitance C, the voltage-controlled full-bridge inverter with a nonlinear inductor is more likely to be unstable. Likewise, in Figure 5, for the load resistance R_L = 5 Ω, the stable region is B_1 + B_2. However, for the load resistance R_L = 10 Ω, the stable region is B_1. Hence, as the load resistance R_L increases, the voltage-controlled full-bridge inverter with a nonlinear inductor has a smaller stable region; that is, the system is more likely to become unstable.

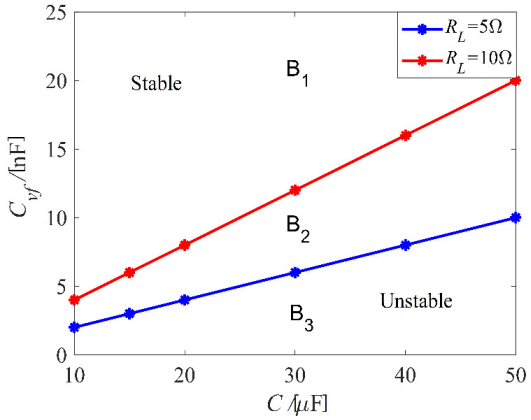

Figure 5. Stability boundaries for various capacitance C_{vf} and capacitance C.

5. Experimental Results

According to the circuit structure given in Figure 2, the designed hardware experimental circuit for the voltage-controlled full-bridge inverter with a nonlinear inductor is shown in Figure 6. In the experiments, the current probe Tek A622 and the voltage differential probe P5200A were used to measure the current and the voltage in the voltage-controlled full-bridge inverter with a nonlinear inductor, and the Tek MDO-34 oscilloscope was used

to capture the waveforms in probes. Four power switches are realized by using IRFP460, and the driver circuit used for driving these four power switches is realized by IR2130, the operational amplifier is LF356, the comparator is LM311, and the phase inverter is MAX628. In addition, the voltage sensor LV25-P (i_P: i_M = 1000: 2500) is used to measure the floating voltage v_0, and its magnification k_M is calculated as follows:

$$k_M = \frac{v_M}{v_0} = \frac{i_M R_M}{i_P R_P} = \frac{2500 \times 200}{1000 \times 2000} = \frac{1}{4} \tag{25}$$

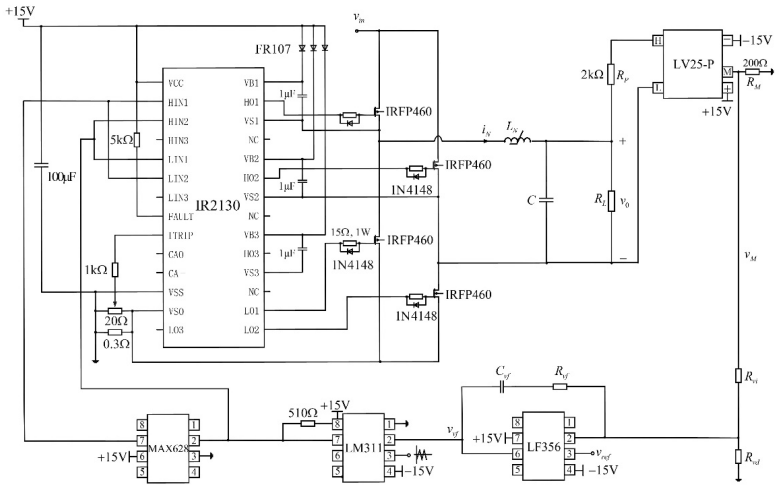

Figure 6. Experimental circuit of the voltage-controlled full-bridge inverter with a nonlinear inductor.

The other parameters remain unchanged, except when choosing a different capacitance, i.e., C_{vf} = 102 nF and C_{vf} = 2 nF, the experimental results of the voltage-controlled full-bridge inverter with a nonlinear inductor can thus be observed. Figure 7a shows the experimental results of the current i_N and the voltage v_0 under C_{vf} = 102 nF. Thus, when C_{vf} = 102 nF, the system is in stable operation. Moreover, the maximum value of the voltage v_0 from the experiment is 7.267 V, and the maximum value of the current i_N in the experiment is 1.522 A. According to (12) and (15), the approximate calculated results for the voltage v_0 and the current i_N are 7.482 V and 1.497 A, respectively. Moreover, by comparing Figure 7a with Figure 3a,b, it can be seen that the experimental results are consistent with the theoretical calculation results, which verifies the correctness of the established model and the effectiveness of the approximate calculations.

In addition, with the aid of the frequency spectrum analysis of the PLECS and choosing 50 Hz as the fundamental frequency, the experimental curves of the current i_N and the voltage v_0 can be obtained, as shown in Figure 7c,d, respectively. One can see that in the range of 0~1 kHz, the harmonics of both the current i_N and the voltage v_0 have smaller amplitudes than the fundamental wave. In the range of 1–2 kHz, the amplitude of each harmonic can be approximately zero.

Figure 8a illustrates the experimental curves of the current i_N and the voltage v_0 under C_{vf} = 2 nF, while Figure 8b is the close-up view of Figure 8a. Figure 8c,d are the harmonic spectrums of the current i_N and the voltage v_0, respectively. It can be seen that when C_{vf} = 2 nF, the voltage-controlled full-bridge inverter with a nonlinear inductor is in unstable operation and there is oscillation; the oscillation frequency is between the power frequency of 50 Hz and the switching frequency of 25 kHz. This oscillation phenomenon can be called medium-frequency oscillation. In the region of the oscillation frequency, both the current i_N and the voltage v_0 have larger harmonics. Therefore, the occurrence of medium-frequency oscillation will increase the difficulty of the system filter design; likewise, will increase the voltage stress and the current stress of the power switches in the system.

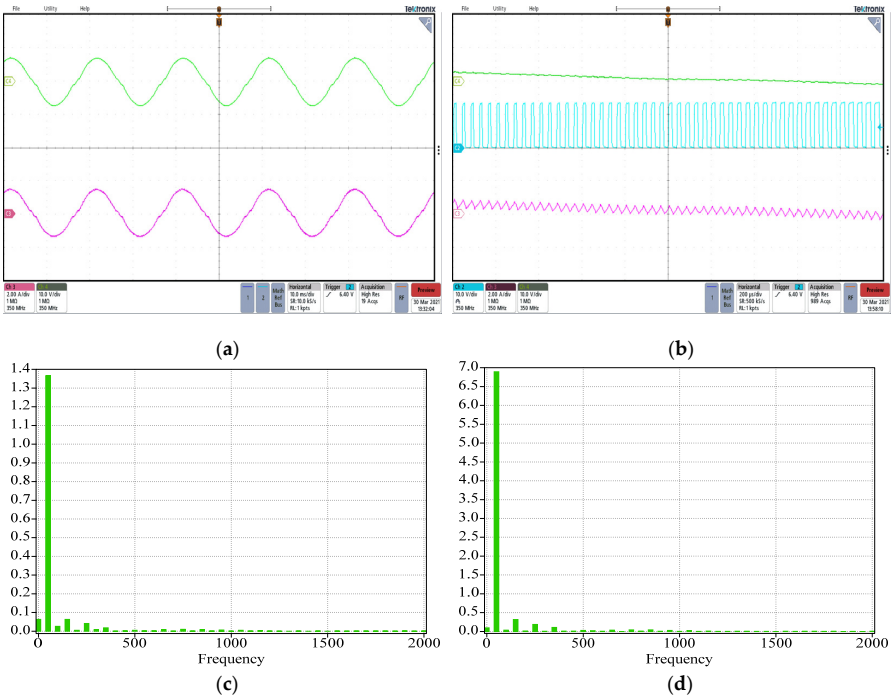

Figure 7. Experiments for C_{vf} = 102 nF. (**a**) v_0 (Ch4: 10 V/div) and i_N (Ch3: 2 A/div), time: 10 ms/div. (**b**) Close-up view, v_0 (Ch4: 10 V/div), i_N (Ch3: 2 A/div), and v_d (Ch2: 10 V/div), time: 200 µs/div. (**c**) Harmonic spectrum of i_N [axis X: Hz, axis Y: A]. (**d**) Harmonic spectrum of v_0 [axis X: Hz, axis Y: V].

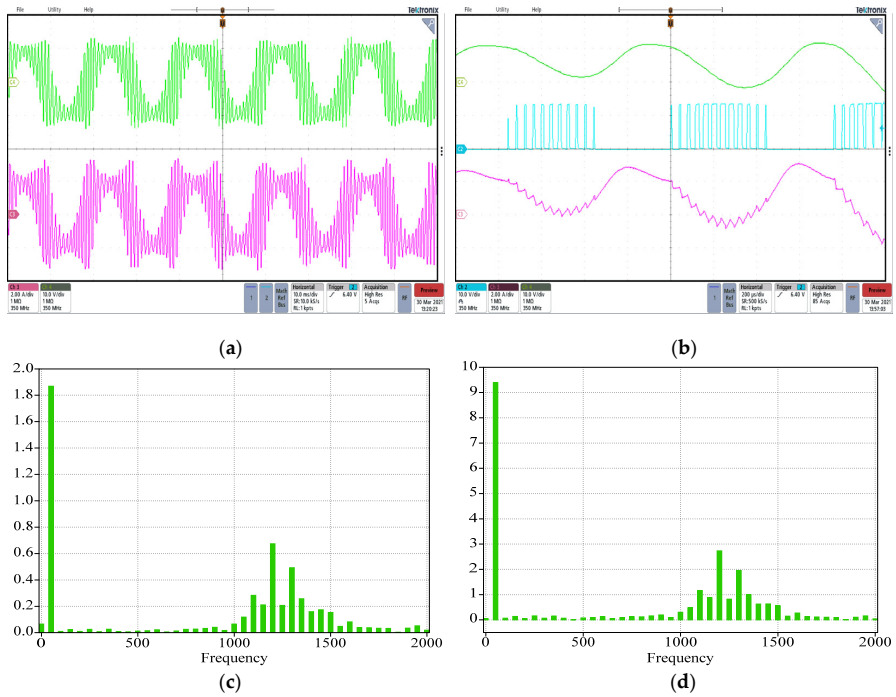

Figure 8. Experiments for C_{vf} = 2 nF. (**a**) v_0 (Ch4: 10 V/div) and i_N (Ch3: 2 A/div), time: 10 ms/div. (**b**) Close-up view, v_0 (Ch4: 10 V/div), i_N (Ch3: 2 A/div), and v_d (Ch2: 10 V/div), time: 200 µs/div. (**c** Harmonic spectrum of i_N [axis X: Hz, axis Y: A]. (**d**) Harmonic spectrum of v_0 [axis X: Hz, axis Y: V].

6. Conclusions

In this paper, the results from theoretical analysis, approximate calculation, stability determination, and circuit experiment show that in the voltage-controlled full-bridge inverter with a nonlinear inductor, the medium-frequency oscillation whose oscillation

frequency is between the power frequency and the switching frequency causes the occurrence of Hopf bifurcation, making the filter design for the system more difficult since this oscillation should be filtered. Hence, the medium-frequency oscillation occurring in the voltage-controlled full-bridge inverter with a nonlinear inductor should be avoided in practical engineering.

Author Contributions: F.W. conceived, validated, and wrote the manuscript. H.Z., J.Z. and H.C. participated in the research plan development and revised the manuscript. All authors have read and agreed to the published version of the manuscript.

Funding: This work was supported in part by the National Natural Science Foundation of China under Grant 51377124.

Conflicts of Interest: The authors declare that there are no conflicts of interest regarding the publication of this paper.

References

1. Luo, F.L.; Hong, Y. *Advanced DC/AC Inverters: Applications in Renewable Energy*; CRC Press Taylor and Francis Group: Boca Raton, FL, USA, 2013; pp. 33–135.
2. Shen, J.L.; Chen, W. Nonlinear analysis and improvement of output filtering inductance for single-phase photovoltaic inverter. *J. Magn. Mater. Dev.* **2020**, *51*, 37–42.
3. Yang, C.Y.; Chen, W. Analysis of effect of ladder gap on nonlinear characteristics of inductors. *J. Power Supply* **2012**, *4*, 39–43.
4. Wang, L.L.; Qiu, Y.J.; Wang, H.L.; Hu, Z.Y.; Liu, Y.F. A new model for designing multiwindow multipermeability nonlinear LTCC inductors. *IEEE Trans. Ind. Appl.* **2015**, *51*, 4677–4686. [CrossRef]
5. Liu, Y.T.; Zhang, D.M. Effect of nonlinear inductor behavior on the performance of interleaved power factor correction. *IEEE Trans. Magn.* **2012**, *48*, 4143–4147. [CrossRef]
6. Alexander, S.; Christof, G. Efficient nonlinear inductors for PV inverters and active PFC. In Proceedings of the 7th International Conference on Integrated Power Electronics Systems, Nuremberg, Germany, 6–8 March 2012; pp. 1–4.
7. Liu, Y.T.; Jiang, S.Q.; Wang, H.Z.; Wang, G.B.; Peng, J.C.; Liu, Y. LCL filter design with the inductor nonlinear behavior consideration in the three phase grid-connected inverter. In Proceedings of the 2018 IEEE International Magnetics Conference, Singapore, 23–27 April 2018; p. 1800026.
8. Mastromauro, R.A.; Liserre, M.; Dell'Aquila, A. Study of the effects of inductor nonlinear behavior on the performance of current controllers for single-phase PV grid converters. *IEEE Trans. Ind. Electron.* **2008**, *55*, 2043–2052. [CrossRef]
9. Li, H.; Zhou, Y.F.; Ling, Q.Q. Modeling and dynamics of boost converter based on nonlinear inductor. *Electr. Meas. Instrum.* **2019**, *56*, 39–44.
10. Sun, L.X.; Zhou, Z.Y.; Wen, Z.G.; Wang, Q.Y. Adaptive carrier amplitude modulation control of bifurcation and chaos in SPWM H-bridge converter. *Electr. Meas. Instrum.* **2020**, *57*, 101–108.
11. Gong, R.X.; Yin, Z.H. A chaos control method of single-phase H-bridge photovoltaic inverter. *Acta Phys. Sin.* **2021**, *70*, 020501.
12. Yang, L.H.; Yang, L.; Yang, F.; Ma, X.K. Slow-scale and fast-scale instabilities in parallel-connected single-phase H-bridge inverters: A design-oriented study. *Int. J. Bifurc. Chaos* **2020**, *30*, 2050005. [CrossRef]
13. Liu, H.C.; Su, Z.X. Study on nonlinear phenomena in dual buck full-bridge inverter. *Acta Phys. Sin.* **2014**, *63*, 010505.
14. Zhang, J.K.; Wu, X.J.; Xing, L.S.; Zhang, C.; Iu, H.; Fernando, T. Bifurcation analysis of five-level cascaded H-bridge inverter using proportional-resonant plus time-delayed feedback. *Int. J. Bifurc. Chaos* **2016**, *26*, 1630031. [CrossRef]
15. Lenz, E.; Pagano, D.J.; Ruseler, A.; Heldwein, M.L. Two-parameter stability analysis of resistive droop control applied to parallel-connected voltage-source inverters. *IEEE J. Emerg. Sel. Top. Power Electron.* **2020**, *8*, 3318–3332. [CrossRef]
16. Chen, Y.; Zheng, Y.; Jiang, L. Nonlinear dynamic behavior of high-frequency isolation quasi-Z-source photovoltaic inverter. *IEICE Electron. Express* **2018**, *15*, 1–12. [CrossRef]
17. Liao, Z.X.; Luo, X.S.; Huang, G.X. Numerical modeling and research on nonlinear dynamic behaviors of two-stage photovoltaic grid-connected inverter. *Acta Phys. Sin.* **2015**, *64*, 130503.
18. Dai, Y.Z.; Zhao, P.C.; Ren, H.J.; Luo, R.Z. Rorder-collision bifurcation and stability domain of non-isolated photovoltaic grid-connected inverter with H6-type. *Acta Energ. Solaris Sin.* **2019**, *40*, 126–133.
19. Asadi, F.; Eguchi, K. *Simulation of Power Electronics Converters Using PLECS*; Elsevier Academic Press: Amsterdam, The Netherlands, 2020; pp. 399–419.
20. Middlebrook, R.D.; Cuk, S. A general unified approach to modelling switching-converter power stages. *Int. J. Electron.* **1997**, *42*, 521–550. [CrossRef]
21. Wang, F.Q.; Zhang, H.; Ma, X.K. Period-doubling bifurcation in two-stage power factor correction converters using the method of incremental harmonic balance and Floquet theory. *Chin. Phys. B* **2012**, *21*, 020505. [CrossRef]